

Performance Characteristics of the Whole-Body Discovery IQ PET/CT System

Gabriel Reynés-Llompart¹, Cristina Gámez-Cenzano¹, Inma Romero-Zayas¹, Laura Rodríguez-Bel¹,
José Luís Vercher-Conejero¹, Josep M Martí-Climent²

¹PET Unit. Nuclear Medicine. IDI. Hospital U. de Bellvitge-IDIBELL, L'Hospitalet de Llobregat,
Barcelona, SPAIN,

²Nuclear Medicine. Clínica Universidad de Navarra, Pamplona, SPAIN.

Disclaimer: Gabriel Reynes-Llompart receives research funding from General Electric Spain.

Corresponding author:

Gabriel Reynés-Llompart

PET Unit. Nuclear Medicine. IDI. Hospital U. de Bellvitge-IDIBELL,
08907 L'Hospitalet de Llobregat, Spain

Tel: 93 264 00 36

Fax: 93 263 05 53

gabriel.reynes@idi.gencat.cat

PhD Student

Words: 4997

Running title: Performance of the Discovery IQ PET/CT

ABSTRACT

Purpose

The aim of this study was to assess the physical performance of a new PET/CT system Discovery IQ 5 Rings (General Electric, Milwaukee, WI).

Methods:

Performance measurements were obtained using the NEMA NU2-2012 methodology. Image quality was extended by accounting for different acquisition parameters (lesion-to-background ratios of 8:1, 4:1 and 2:1 and acquisition times) as well as different reconstruction algorithms (VPHD, VPHD-S and Q.Clear). Tomographic reconstruction was also assessed using a Jaszczak phantom. Additionally, a total of thirty patient lesions were analyzed to account for differences on reconstruction algorithms in terms of lesion volume and SUV quantification.

Results:

Spatial resolutions ranged from 4.2 mm at 1 cm to 8.5 mm at 20 cm. Sensitivity measured in the center and at 10 cm was 22.8 and 20.4 kps/kBq, respectively. The measured noise equivalent count rate (NECR) peak was 124 kcps at 9.1 kBq/cm³. The scatter fraction was 36.2%. The accuracy of correction for the count losses and randoms was 3.9%. In the image quality test the contrast recovery for VPHD/VPHDS/Q.Clear ranged between 18/18/13% (hot contrast, 10 mm sphere diameter, ratio of 2:1) and 68/67/81% (cold contrast, 37 mm sphere diameter, ratio of 8:1). The background variability was between 3.4/3.0/2.1% (ratio 2:1) to 5.5/4.8/3.7% (ratio 8:1). On Q.Clear reconstruction, the decrease of the β value has the effect of increasing the contrast recovery coefficients and the background variability. The Jaszczak phantom presented an overall image quality increase when using a reconstruction algorithm that models the point-spread function, moreover Q.Clear increased signal-to-noise ratio. Lesions analyzed for VPHD-S and Q.Clear presented a SUV_{mean} of 6.5±3 and 7±3 (p<0.01), respectively, and a SUV_{max} of 11±4.8 and 12±4 (p<0.01). No significant lesion mean volume differences were found between algorithms.

Conclusions:

Discovery IQ PET/CT with 5 ring block detectors has the highest overall performance of the Discovery BGO based scanners, with improved sensitivity and count rate performance. The Q.Clear

reconstruction improves the PET image quality, with higher recovery coefficients and lower background variability.

Key word: PET/CT, Discovery-IQ, NEMA NU 2-2012, Q.Clear

INTRODUCTION

Positron emission tomography (PET) imaging has the ability to offer valuable functional information, playing a key role in the diagnosis, staging and evaluation of cancer, radiotherapy planning or diagnosis of some dementia pathologies (1). PET scanner performance has improved in hardware and reconstruction methods (2). Since the introduction of the hybrid PET computed tomography (PET/CT) scanners and especially with the last generation tomographs, most commercial manufacturers have opted to include high time resolution detectors, based on LSO (3,4) and LYSO (5-8) crystals, in order to obtain a better time of flight localization. However, GE Healthcare maintains a line of PET/CT scanners based on Bismuth Germanium Oxide (BGO) detectors (9,10), opting for a higher sensitivity at a lower detector price. Higher PET scanner sensitivity has been also achieved by adopting the 3D mode operation, without any interplane septa, which increases sensitivity by a factor of 4 to 6 as compared with the 2D mode (2). An additional method to improve sensitivity is to extend the axial field of view (FOV), hence an 81% in sensitivity gain has been reported (11).

Recently GE HealthCare has renewed the scanner design in the Discovery IQ (D-IQ) from its non-time-of-flight PET/CT scanner series, introducing a new configuration of the block detector, which allows increasing the number of detector rings from three to five along the axial FOV, and hence improving the system sensitivity. The scanner also includes a new reconstruction algorithm, the Q.Clear, which has been shown to significantly improve signal-to-noise ratio and Standardized Uptake Value (SUV) quantification in a Lutetium-Yttrium Oxyorthosilicate (LYSO) PET/CT scanner (6), when compared to an Ordered Subset Expectation Maximization (OSEM) algorithm.

The purpose of this study was firstly to evaluate the physical performance of a new D-IQ PET/CT with its 5 rings configuration. We mostly used the NEMA NU2-2012 (12), which represents the gold standard for acceptance testing and comparison of different systems, and some additional tests. Secondly, we evaluated the possible advantages of using the reconstruction algorithm Q.Clear in both phantoms and clinical images.

MATERIALS AND METHODS

Discovery IQ PET/CT

The Discovery IQ with 5 rings system (D-IQ-5) (GE Healthcare, Milwaukee, WI, USA) combines a BGO based PET tomograph with a 16-slice CT scanner. In its 5 rings configuration, the D-IQ PET enables an axial and transaxial physical FOV of 26 cm and 70 cm respectively, with 79 image planes and 3.27 mm plane spacing. The typical bed overlap is in the range of 19% to 24% (representing 50 to 60 mm). The LightBurst detector unit included has 5 blocks of detectors in the axial direction, consisting of BGO crystals with a size of 6.3 x 6.3 x 30 mm, configuring an 8 x 8 matrix for each block. The scanner has 36 detector units per ring and in total 720 photomultipliers. The ring diameter is 74 cm. The coincidence window is 9.5 ns, and the lower and higher energy thresholds are 425 and 650 keV. GEMS introduced a dual acquisition channel to optimize the performance in low/high-count rate acquisitions, reducing the dead time losses and pileup. In addition, each block detector includes four temperature sensors, to model the performance of the detection on temperature variations. The system allows three-dimensional (3D) and four-dimensional (4D) acquisition modes with an axial coincidence acceptance of ± 39 planes.

Regarding the CT scanner, it can cover a scan FOV of 50 cm and a reconstruction FOV of 70 cm to match PET images. Also, the HiLight Matrix II detector, with 21888 elements, consists in 24 detector rows, 16 rows of 0.625 mm and 8 rows of 1.25 mm, covering 20 mm.

Reconstruction algorithms

The D-IQ-5 software includes two principal algorithms, the VUE-point HD (VPHD) and the Q.Clear. VPHD uses a fully 3D maximum likelihood ordered subsets-expectation maximization (OSEM) with corrections for scatter and random coincidences, dead time, attenuation, and normalization incorporated into the iterative reconstruction. It also has the option to include a point spread function modeling (PSF) (13), conforming the VPHD-S reconstruction. Variable parameters

are iterations, subsets and filtering. It can be specified an in-plane Gaussian filter with a specified cut-off value and a Z-Axis filter (defined as Light, Standard or Heavy).

Q.Clear is the commercial name for a Bayesian penalized likelihood reconstruction algorithm, available in the new generation of GEMS PET/CT scanners. It includes a PSF modeling and a regularization controlled by a penalty term (β), which is the only user input. The penalty function acts as a noise suppression term (14), a more detailed description can be found on Supplemental Material. Filter back projection is not included as a reconstruction method.

PET scanner performance evaluation

The performance of the PET scanner was conducted mainly following the NEMA NU 2-2012 standard (12), using the software included in the scanner and in-house software. The different tests are briefly described, as well as the changes introduced to extend them.

Spatial resolution

Spatial resolution is a measure of the ability to distinguish between two points after the image is reconstructed. Measurements were performed by preparing three hematocrit capillary tubes filled with a point like ^{18}F drop. The prepared point sources were less than 1 mm of diameter, and the activity in each drop was approximately 4.5 MBq. Using a source holder, they were placed and acquired fulfilling NEMA specifications (12).

Data were reconstructed using the VPHD algorithm (matrix size 256 x 256, FOV 25, 12 iterations, 12 subsets, 2 mm cut off Gaussian filter). Spatial resolution was calculated as full-width at half-maximum (FWHM) and full-width at tenth-maximum (FWTM) of the reconstructed PSF using a vendors software.

Sensitivity

The sensitivity test measures the rate of coincidence detection events that the scanner makes for every unit of activity in the FOV. Measurements were made with different amounts of attenuating material, with the results extrapolated to give the scanner sensitivity with no attenuating material. The random coincidences were subtracted from prompts to obtain the trues-only sensitivity results.

We used the NEMA PET sensitivity phantom (Data Spectrum Corp., Hillsborough, NC) which meets NEMA specifications (12). The tube was filled with 3.33 MBq of ^{18}F , in order to assume that count losses are negligible. For each sleeve surrounding the line source, successive measurements were acquired with the phantom suspended in the center of the transaxial FOV and at a radial distance of 10 mm from the scanner axis. For each aluminum sleeve, data were acquired for 60 s.

Scatter Fraction and Count rate Performance

The count losses and random portion of this test measures the count rate performance of the scanner as a function of the present activity; and the scatter fraction measures the relative system sensitivity to scattered radiation.

The phantom used agreed NEMA specifications (12). The line source was filled with an activity concentration of approximately 50 MBq/mL at the time of acquisition. Data were acquired during 17.5 h resulting in 36 frames. Frames from 1 to 20 were acquired consecutively with a time of 15 min/frame. Frames from 21-25 were acquired for 25 min/frame with a delay of 25 min between each consecutive pair of frames. The remaining two frames were acquired as the last group (25 min/frame), but without delay. The scatter fraction and the noise equivalent count rate (NECR) were determined as described in the NEMA NU2-2012 standard using software tools provided by the manufacturer.

Accuracy of Count Losses and Random Corrections

The accuracy of count losses and random corrections was measured by comparing the true rate calculated using count losses and random corrections, with the true rate extrapolated from a weighted least-square fit assuming negligible count losses and random. Data recorded for the scatter fraction and count rate test were reconstructed with an 18 cm FOV in a 128x128 matrix, using the VPHD algorithm (with 2 iterations, 12 subsets, a Gaussian 6.4 mm cut off filter and a Z-Axis Standard filter) and corrected for dead time, random, scatter and attenuation.

Image Quality

The NEMA IEC body phantom, consisting of six spheres with diameters of 10, 13, 17, 22, 28 and 37 mm, a cylindrical lung insert, and the NEMA scatter phantom were used for the evaluation of the image quality. Both phantoms were positioned according to NEMA standards (12). The activity in the line source of the scatter phantom was 100 MBq at the start of the first acquisition. The IEC body phantom was filled with an initial radioactivity concentration of 5.5 kBq/cm³. The two biggest spheres were filled with non-radioactive water, and the remaining spheres with a lesion-to-background ratio (LBR) of 4:1 and 8:1, as stated by the NEMA test, and 2:1. Three sequential measurements of 350 s each were acquired for a single-bed position in list mode.

All data were corrected for random coincidences, normalization, dead time losses, scatter, and attenuation. For the reconstruction we used the manufacturer's algorithms VPHD and VPHD-S, both reconstructed using a clinical protocol of 4-iterations, 12-subsets and a 4.8 mm Gaussian filter, as well as Q.Clear with a beta value of 350 (matrix = 256 x 256, FOV = 70 cm). To evaluate the effect of the reconstruction parameters, images were also reconstructed with the following settings: Q.Clear with a β of 50, VPHD and VPHD-S using 12 subsets, 8 iterations and a 2.0 mm Gaussian filter.

Image quality test acquisition time and reconstruction parameters were those suggested by the PET scanner manufacturer for the acceptance test, and they do not reproduce our clinical setting for a 70 kg patient with an activity injected of 185 MBq and an acquisition of 2 minutes per bed position. Then, from the phantom list mode acquisitions three 60 s frames were generated to

simulate the same statistics acquisition as it is produced for a patient, and the images were reconstructed using the Q.Clear algorithm with a beta value of 350. Data processing was performed using custom in-house software developed in MATLAB following NEMA specifications to obtain cold and hot contrast recovery (CR) coefficients, lung residual error and background variability (BV).

An extension of the image quality performance tests using the Jaszczak phantom was performed and described on Supplemental Material.

Patient studies

A total of 30 lesions from 16 different patients, were analyzed in order to account differences between algorithms in the evaluation of clinical SUV values in ^{18}F -FDG studies. Administered activity was 2.5 MBq/kg and images were acquired after 60 minutes of injection. Acquisition time was 2 min per bed position. Images were reconstructed (matrix = 256 x 256, FOV = 70 cm) using VPHD-S (4-iterations, 12-subsets, 4.8 mm filter, Z-Axis Standard filter) and Q.Clear (beta = 350). For each patient, lesions were analyzed drawing a volume of interest (VOI) using a segmentation threshold of 41%, by means of the maximum (SUV_{max}) and mean (SUV_{mean}) standard uptake, and by lesion volume (corresponding to the segmented volume). In addition, a spherical VOI of 5 cm³ was positioned upon the healthy liver to account for differences on possible noise variability; the noise was defined as the ratio of SUV_{mean} by the standard deviation of the uptake in the liver VOI (15). Data normality was determined by using the Shapiro-Wilks test. The paired two-tailed Student's t-test was used to compare the lesion parameters obtained from the VPHD-S and Q.Clear reconstructions.

RESULTS

Scanner performance

The tangential, axial and radial resolutions for the different positions of the point source, reconstructed using the clinical VPHD algorithm, are summarized in Table 1, lists FWHM and

FWTM values for 1, 10, and 20 cm as an average over both axial positions stated by NEMA procedure. The sensitivity at the center was 22.80 cps/kBq and 20.43 cps/kBq at 10 cm. Fig. 1 presents sensitivity slice profile depending on the offset.

The peak NECR was 123.6 kcps at a concentration of 9.1 kBq/mL. The scatter fraction measured at the NECR peak was 36.2%. The peak of true count rate was at 490.1 kcps at 25.8 kBq/mL. NECR curve and count rate values as a function of the activity are presented in Fig. 2 including true, random and scatters events as well as total prompts. The maximum absolute error below the NECR peak was 3.9%. For the true rate versus the effective activity concentration, Fig. 3 presents the maximum, mean and minimum errors for all activity concentrations.

Fig. 4 shows the images obtained for the NEMA image quality phantom. Images reconstructed with the Q.Clear algorithm present less background variability, especially as the LBR decreases. Tables 2, 3 and 4 present NEMA image quality data at LBR of 2:1, 4:1 and 8:1, respectively, for the VPHD, VPHDS and Q.Clear reconstructions. Results are presented as mean and standard deviation of the three measurements requested by NEMA standard. Q.Clear presents a higher CR and lower BV. Although, for this reconstruction, the smallest sphere (10 mm) for the 2:1 and 4:1 LBR had the lowest CR factor, this fact was compensated with a lower BV that results in an increased the signal-to-noise ratio, as seen in Fig. 4. Additionally, decreasing the β value in the Q.Clear reconstruction or increasing the effective number of iterations in the VPHD and VPHD-S and reducing Gaussian filtering, increases the hot CR of the smaller spheres (10-17 mm) as expenses of a BV increase, Supplemental Table 1-3. For the lung residual error for scatter attenuation corrections, Q.Clear presents the lower values for all LBR studied. Also, in Q.Clear reconstructions, when the product of the acquisition time and the activity concentration in the phantom is adjusted to meet the clinical situation (60 s for a 5.5 kBq/cm³ concentration) the CR coefficients are about the same for a given sphere diameter and LBR (Table 5). In contrast, the BV increases for the short acquisition (from a mean value of 2.7 to 5.1 %, considering all spheres and LBR), with a more noticeable difference among spheres and LBR values.

Results of the image quality tests with different reconstruction parameters are presented in the supplementary material. In the Q.Clear reconstruction, the decrease of the β value has the effect of increasing the CR coefficient and the BV, in the same way as an increase of effective iterations does in the VPHD and VPHD-S reconstructions.

Measurements with the Jaszczak phantom (Supplemental Figs. 1 and 2) showed that the incorporation of PSF in the reconstruction, the overall image quality increases; but the Q.Clear algorithm allows a better definition of the 7.9 mm rods and provides the best image contrast for all the rod sets, reducing image noise.

Patient studies

The 16 patients had a mean weight of 69 ± 14 kg, and the mean administered activity was 187 ± 38 MBq. Q.Clear and VPHD-S reconstruction times were about 5 min/bed and 2 min/bed, respectively. Overall, image quality was comparable for VPHD-S and Q.Clear reconstruction, but the later had a better contrast. When images were analyzed by an expert nuclear medicine physician, only encountered relevant visual differences in image quality of the patient scans with small lesions (Fig. 5). The quantitative analysis of the VOIs, showed that for VPHD-S and Q.Clear the mean lesion volume were 7 ± 11 and 7 ± 13 cm³ ($p=0.5$), the SUV_{mean} were 6.5 ± 3 and 7 ± 3 ($p<0.01$) and the SUV_{max} were 11 ± 4.8 and 12 ± 4 ($p<0.01$). Fig. 6 presents individual tendencies and boxplots for the three parameters. Two lesions presented a lower SUV for Q.Clear than VPHD-S. Between the two reconstruction methods, mean variation of SUV_{mean} was $13 \pm 10\%$ (maximum 35%), and of SUV_{max} was $9 \pm 12\%$ (maximum 29%). Liver VOIs mean noise was 0.12 ± 0.03 for VPHD-S, and 0.11 ± 0.05 for Q.Clear ($p=0.09$). See Supplemental Fig. 3 for the SUV_{mean} on liver VOI.

DISCUSSION

D-IQ is the latest generation of the BGO PET/CT scanners developed by General Electric Medical Systems, following the Discovery-LS (16), Discovery-ST (17,18), Discovery-STE (9) and

Discovery-600 (10) series. It can be configured with two to five block detector rings with an axial FOV from 10.4 to 26.0 cm. The scanner also includes Q.Clear, a Bayesian penalized likelihood reconstruction algorithm that also incorporates the PSF modeling. In the present study, we evaluated the D-IQ scanner performance in its 5 ring configuration. The main improvement as compared with the previous generation Discovery-600 (D-600) series is the LightBurst PET detector technology (10). That, besides allowing the scalability to different axial FOV, incorporates a dual channel acquisition technology, four temperature sensors in each block detector and an improved detector shielding to reduce scatter photons detection.

Spatial resolution was measured on images reconstructed with an iterative algorithm (VPHD), as the images of the point source were acquired and reconstructed with the patient dedicated software, not allowing a filtered back projection reconstruction. Thus, the comparison with the D-600 series performance published data is difficult. Theoretically, as the crystal size in the transaxial direction was increased in the D-IQ, it should result in a poorer transverse spatial resolution, whereas the axial resolution should be comparable.

D-IQ-5 sensitivity (21.6 cps/kBq) is twice that of D-600 (9.6 cps/kBq). The former presents a smaller ring detector diameter with respect to the D-600, which should provide a small increase of the sensitivity. Furthermore, the major contribution to the D-IQ-5 sensitivity gain arise from an extended axial FOV (from 15.3 to 26 cm), as a consequence of the increased number of detector rings, from three to five, in the D-IQ-5.

D-IQ scanners incorporate a dual integration channel acquisition technology that improves the scatter and count rate performance. SF for D-IQ-5 and D-600 are similar (36.2 and 36.6 % respectively). Although both scanners have the same lower energy threshold (425 keV), two factors should contribute to a higher SF: D-IQ-5 has a smaller ring diameter (74 vs 80.1 cm) and a longer axial length. In addition, the D-IQ-5 has additional end and front shielding specially designed to reduce scatter out of the FOV, and a tungsten shield was designed to reduce the cross-crystal scatter. The true rate and NECR peaks are 46% and 64% higher for the D-IQ-5 compared to the D-600 (335.4 cps @33.2 kBq/mL and 75.2 kcps @12.9 kBq/mL), at a slightly lower activity

concentrations. The maximum absolute error at activity below NEC peak was slightly worse than for the D-600 (2.9%). The peak in the sensitivity profile is produced by the axial coincidence acceptance, allowing coincidences among all the detectors along the scanner axis, similar to the D-600, and changing from older scanners where a full 3D acquisition was not allowed. This profile variability is compensated with the overlap between bed acquisitions.

Results of the image quality test cannot be compared in a straightforward way with other scanners, due to differences in image processing and in the acquisition time. In the present study, guidelines suggested by GE Healthcare were followed; in addition, a more realistic condition with a worse combination of acquisition time and phantom activity concentration was simulated. In that situation, sphere CR coefficients remained at about constant levels, while BV increased. The introduction of the Q.Clear reconstruction improves noticeably the image quality, increasing the CR coefficients and decreasing the BV. These are consistent with previous results from the Discovery 960 scanner based on LYSO crystals (6). Image quality results suggest the need of further investigation on the optimization of the reconstruction parameters, particularly of the β parameter in the Q.Clear reconstruction, for specific clinical applications, as for low count PET acquisitions, due to short acquisition times or low activity administrations.

The patient images reconstructed with the Q.Clear algorithm showed a higher contrast, with less BV. The same improvement is present in the images of the Jaszczak and NEMA image quality phantoms. In the first case, it can be appreciated a better definition up to the 7.9 mm rods. No relevant difference of the noise measured in the liver was observed, although Q.Clear reconstructions presented a slightly lower value. For lesion quantification, the Q.Clear reconstruction increased lesions SUV mean and maximum. These changes in PET quantification introduced by the algorithm election and settings should be considered, especially when standardization and harmonization is required as for multicenter studies (19). A major drawback of the Q.Clear reconstruction was the increase on the reconstruction time.

There are several limitations in this study. Scanner performance evaluation according NEMA NU-2-2012 was adapted, requiring filter back projection, although this reconstruction method is not

implemented in the D-IQ-5 scanner tested. In addition, further studies are needed to evaluate the impact of the Q.Clear reconstruction in the Discovery BGO based scanners, especially for low activity protocols where the high scanner sensitivity should be exploited.

CONCLUSIONS

D-IQ PET/CT with 5 ring block detectors has the highest overall performance of the Discovery BGO based scanners, with improved sensitivity and count rate performance. The Q.Clear reconstruction improves the PET image quality, with higher recovery coefficients and lower background variability.

DISCLOSURE STATEMENT

Gabriel Reynes-Llompart receives research funding from General Electric Spain. All other authors declare none conflict of interests.

REFERENCES

1. Ell PJ. The contribution of PET/CT to improved patient management. *Br J Radiol.* 2006;79:32-36.
2. Slomka PJ, Pan T, Germano G. Recent advances and future progress in PET Instrumentation. *Semin Nucl Med.* 2015;46:5-19.
3. Martí-Climent JM, Prieto E, Domínguez-Prado I, et al. Contribution of time of flight and point spread function modeling to the performance characteristics of the PET/CT Biograph mCT scanner. *Rev Esp Med Nucl Imagen Mol.* 2013;32:13-21.
4. Rausch I, Cal-González J, Dapra D, et al. Performance evaluation of the Biograph mCT Flow PET/CT system according to the NEMA NU2-2012 standard. *EJNMMI Phys.* 2015;2:26.
5. Bettinardi V, Presotto L, Rapisarda E, Picchio M, Gianolli L, Gilardi MC. Physical performance of the new hybrid PET/CT Discovery-690. *Med Phys.* 2011;38:5394.
6. Teoh EJ, McGowan DR, Macpherson RE, Bradley KM, Gleeson F V. Phantom and clinical evaluation of the bayesian penalized likelihood reconstruction algorithm Q.Clear on an LYSO PET/CT System. *J Nucl Med.* 2015;56:1447-1452.
7. Kolthammer JA, Su K-H, Grover A, Narayanan M, Jordan DW, Muzic RF. Performance evaluation of the Ingenuity TF PET/CT scanner with a focus on high count-rate conditions. *Phys Med Biol.* 2014;59:3843-3859.
8. Miller M, Zhang J, Binzel K, et al. Characterization of the Vereos digital photon counting PET system. *J Nucl Med.* 2015;56:434-434.
9. Teräs M, Tolvanen T, Johansson JJ, Williams JJ, Knuuti J. Performance of the new generation of whole-body PET/CT scanners: Discovery STE and Discovery VCT. *Eur J Nucl Med Mol Imaging.* 2007;34:1683-1692..
10. De Ponti E, Morzenti S, Guerra L. Performance measurements for the PET/CT Discovery-600 using NEMA NU 2-2007 standards. *Med Phys.* 2011;38:968-974.
11. Jakoby BW, Bercier Y, Watson CC, Bendriem B, Townsend DW. Performance

- characteristics of a new LSO PET/CT scanner with extended axial field-of-view and PSF reconstruction. *IEEE Trans Nucl Sci.* 2009;56:633-639.
12. *National Electrical Manufacturers Association. Performance Measurements of Positron Emission Tomographs. NEMA Standards Publication NU 2-2012.* Rosslyn, USA; 2012.
 13. Rahmim A, Qi J, Sossi V. Resolution modeling in PET imaging: theory, practice, benefits, and pitfalls. *Med Phys.* 2013;40:64301.
 14. Ahn S, Ross SG, Asma E, et al. Quantitative comparison of OSEM and penalized likelihood image reconstruction using relative difference penalties for clinical PET. *Phys Med Biol.* 2015;60:5733-5751.
 15. Lois C, Jakoby BW, Long M J, et al. An assessment of the impact of incorporating time-of-flight information into clinical. 2010;51:237-245.
 16. Bolard G, Prior JO, Modolo L, et al. Performance comparison of two commercial BGO-based PET/CT scanners using NEMA NU 2-2001. *Med Phys.* 2007;34:2708.
 17. Bettinardi V, Danna M, Savi A, et al. Performance evaluation of the new whole-body PET/CT scanner: Discovery ST. *Eur J Nucl Med Mol Imaging.* 2004;31:867-881.
 18. Mawlawi O, Podoloff D a, Kohlmyer S, et al. Performance characteristics of a newly developed PET/CT scanner using NEMA standards in 2D and 3D modes. *J Nucl Med.* 2004;45:1734-1742.
 19. Boellaard R, Delgado-Bolton R, Oyen WJG, et al. FDG PET/CT: EANM procedure guidelines for tumour imaging: version 2.0. *Eur J Nucl Med Mol Imaging.* 2015;42:328-354.

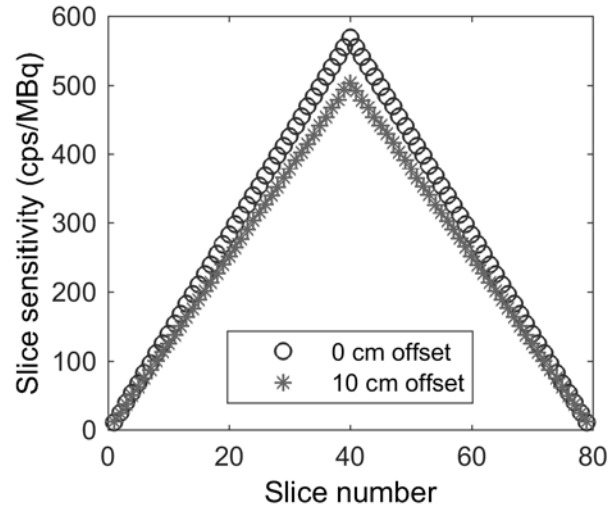


FIGURE 1. Axial sensitivity profile for the measurements in the center of the field of view and at 10 cm radial offset.

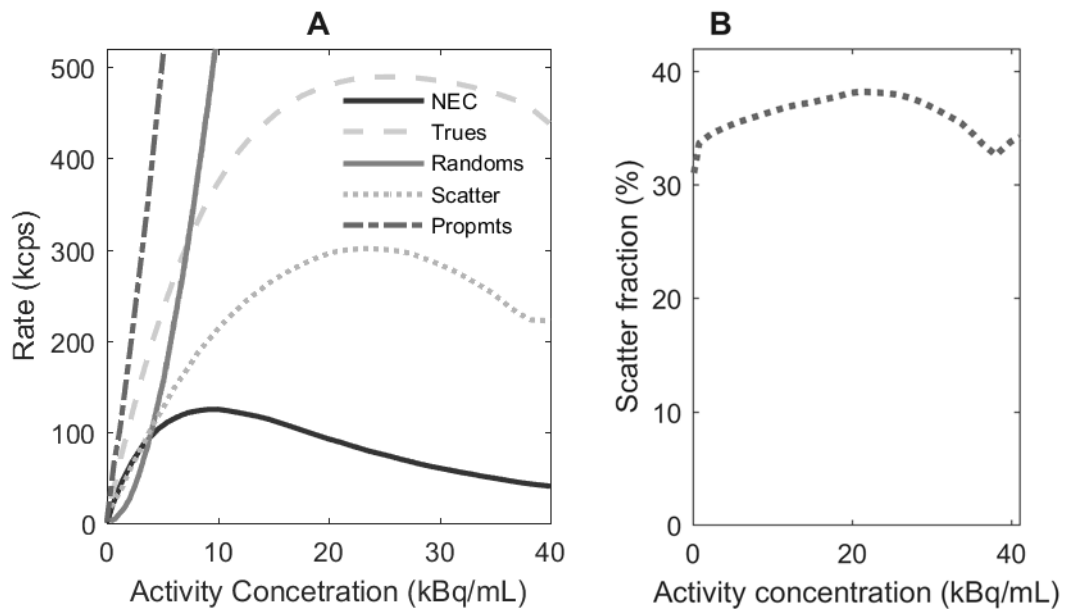


FIGURE 2. Count rate performance: (A) Count rate curves for true, random, scatter and total events and NECR curve as a function of the activity concentration. (B) Scatter fraction as a function of the activity concentration.

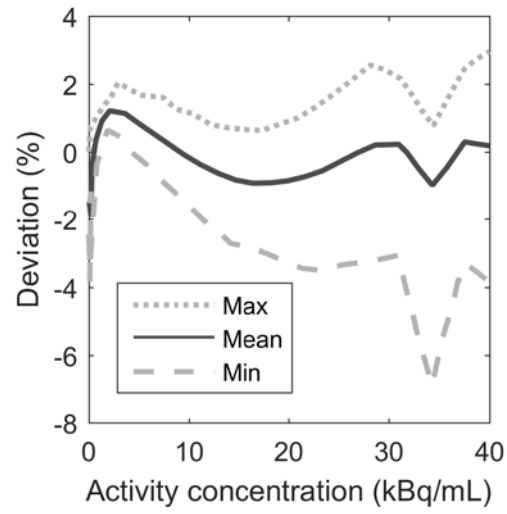


FIGURE 3. Count rate accuracy: maximum, mean and minimum error as a function of the activity concentration.

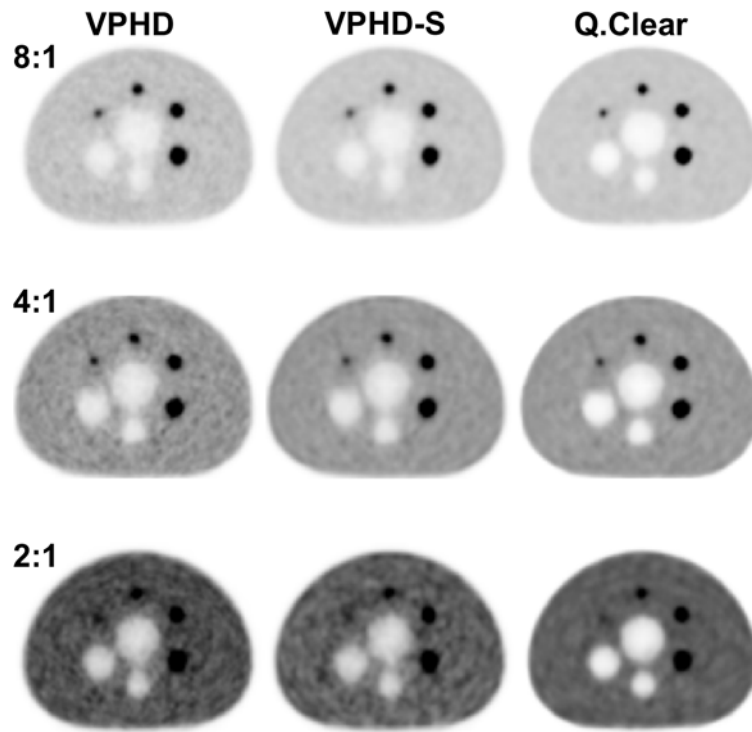


FIGURE 4. Central slice from the NEMA IEC body phantom. Image quality test for L/B = 8:1, 4:1 and 2:1 in (from top to bottom). Reconstructed images with the VPHD, VPHD-S and Q.Clear reconstruction algorithms (from left to right).

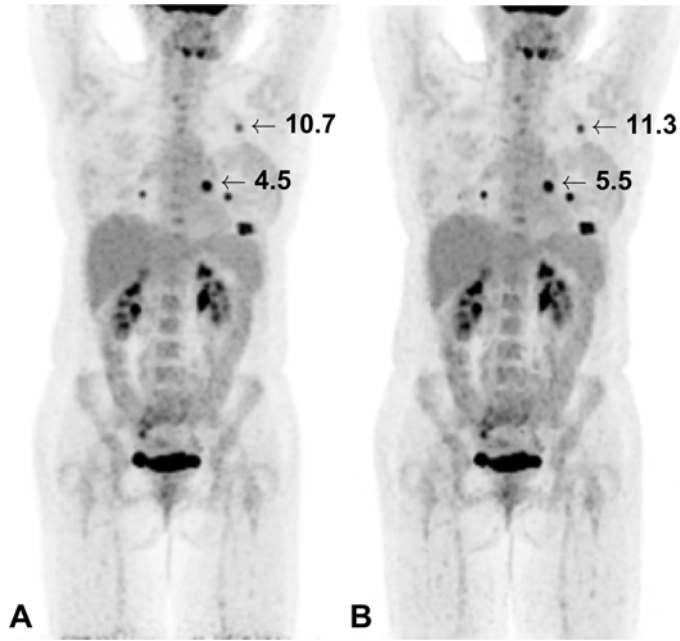


FIGURE 5. Maximum intensity projection of a patient scan reconstructed using (A) VPHD-S, and (B) Q.Clear. The numbers indicate the SUV_{max} of the analyzed lesions.

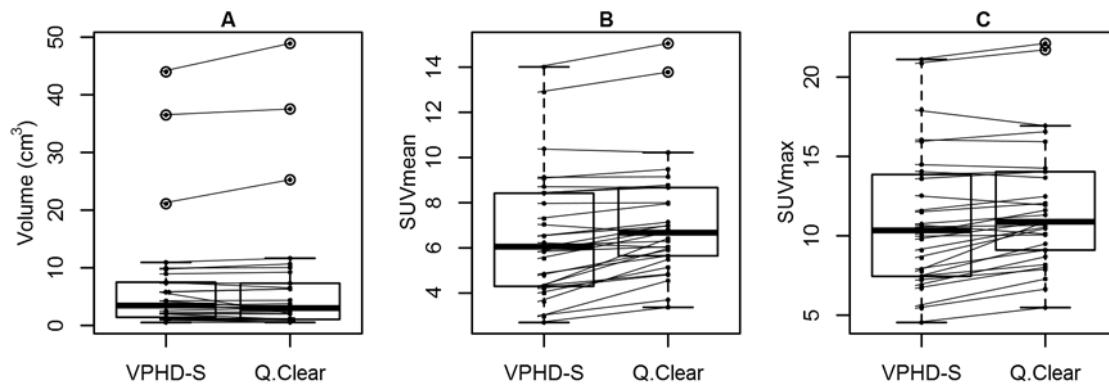


FIGURE 6. Quantitative analysis of the analyzed lesions for VPHD-S and Q.Clear reconstructions.

Measured values of (A) volume, (B) SUV_{mean}, and (C) SUV_{max},

TABLE 1. Spatial resolution measured for D-IQ-5 PET system according to NEMA procedure using VPHD iterative reconstruction.

Distance (cm)	Radial		Tangential		Axial	
	FWHM	FWTM	FWHM	FWTM	FWHM	FWTM
	(mm)	(mm)	(mm)	(mm)	(mm)	(mm)
1	4.2	9.5	4.7	9.8	4.8	11.2
10	5.6	11.4	5.1	10.2	4.8	11.1
20	8.5	15.2	5.5	11.2	4.8	11.7

TABLE 2. Image quality comparison using NEMA NU2-2012 for different reconstruction algorithms (256x256 matrix) and a lesion-to-background of 2:1. Q.Clear with a β of 350, VPHD and VPHD-S using VPHD and VPHD-S with 4-iterations, 12-subsets and a 4.8 mm Gaussian filter.

Sphere diameter (mm)	Contrast Recovery (%)			Background Variability (%)		
	VPHD	VPHDS	Q.Clear	VPHD	VPHDS	Q.Clear
10	18±4	18±2	13±1	4.4±0.9	3.5±0.8	2.5±0.6
13	37±3	35±2	33±1	4.0±0.6	3.3±0.7	2.3±0.5
17	59±4	60±3	60±2	3.6±0.4	3.1±0.5	2.2±0.4
22	70±4	72±3	75±1	3.4±0.3	3.0±0.3	2.1±0.3
28	61±1	61±1	71.1±0.3	3.3 ±0.3	3.0±0.3	2.2±0.2
37	64±2	64±1	77±1	3.5±0.3	3.2±0.3	2.6±0.1
Lung residual (%)	-	-	-	26±0.3	26.8±0.2	11.8±0.3

TABLE 3. Image quality comparison using NEMA NU2-2012 for different reconstruction algorithms (256x256 matrix) and a lesion-to-background of 4:1. Q.Clear with a β of 350, VPHD and VPHD-S using VPHD and VPHD-S with 4-iterations, 12-subsets and a 4.8 mm Gaussian filter.

Sphere diameter (mm)	Contrast Recovery (%)			Background Variability (%)		
	VPHD	VPHDS	Q.Clear	VPHD	VPHDS	Q.Clear
10	25±3	20±3	22±3	5.5±0.3	4.2±2.5	3.3±0.4
13	40±3	37±1	44±1	4.9±0.3	3.8±2.2	3.0±0.3
17	61±2	62±1	68±1	4.2±0.3	3.3±1.8	2.0±1.0
22	68±1	71±1	76±1	3.6±0.2	2.8±1.5	2.5±0.1
28	64±1	63±1	73±1	3.4±0.3	2.8±1.2	2.5±0.1
37	68±1	67±1	81±1	3.3±0.1	2.8±0.7	2.7±0.2
Lung residual (%)	-	-	-	22.2±0.1	22.9±0.4	9.3±0.7

TABLE 4. Image quality comparison using NEMA NU2-2012 for different reconstruction algorithms (256x256 matrix) and a lesion-to-background of 8:1. Q.Clear with a β of 350, VPHD and VPHD-S using VPHD and VPHD-S with 4-iterations, 12-subsets and a 4.8 mm Gaussian filter.

Sphere diameter (mm)	Contrast Recovery (%)			Background Variability (%)		
	VPHD	VPHDS	Q.Clear	VPHD	VPHDS	Q.Clear
10	31±2	30±2	33±3	5.5±0.8	4.8±0.6	3.7±0.1
13	44±1	49±1	51±1	5.0±0.6	4.4±0.5	3.4±0.1
17	57±2	67±2	70±1	4.5±0.3	3.9±0.3	3.1±0.2
22	67±1	70±1	77.5±0.4	3.9±0.2	3.5±0.2	2.9±0.2
28	60±3	60±2	68±2	3.4±0.2	3.4±0.1	2.7±0.1
37	63±2	62±2	77.3±1	3.5±0.3	3.8±0.1	3.0±0.1
Lung residual (%)	-	-	-	25.5±0.3	26.5±0.4	11.5±0.5

TABLE 5. Image quality evaluation of Q.Clear algorithm with a 60 s acquisition using NEMA NU2-2012 for lesion-to-background ratios of 8:1, 4:1 and 2:1.

Sphere diameter (mm)	Contrast Recovery (%)			Background Variability (%)		
	8:1	4:1	2:1	8:1	4:1	2:1
10	36±3	25±3	17±4	9±0.1	7.0±0.3	10.4±0.8
13	48±5	44±5	27±2	8±0.1	6.2±0.1	8.8±0.6
17	70±4	63±4	66±4	7±0.2	5.3±0.1	7.2±0.5
22	73±1	72±1	79±5	6±0.3	4.4±0.3	5.9±0.6
28	68±1	72±1	72±3	5±0.4	3.6±0.3	5.1±0.4
37	79±1	74±1	77±2	4±0.5	3.±0.1	4.5±0.3
Lung residual (%)	-	-	-	12±0.4	10.5±0.6	12.3±0.5

Supplemental Data

A. Description of the Discovery IQ PET/CT

A. Extended explanation of Q.Clear reconstruction

Q.Clear uses a block sequential regularized expectation maximization (BSREM) method for reconstruction. It includes a point-spread function (PSF) modeling and controls the noise through the use of a penalty term¹. The penalty term imposes more smoothing in lower activity regions and less smoothing in higher activity regions, resulting in smoother cold backgrounds and improved hot lesions signal-to-noise ratios. At the same time, the use of the penalty function, allows an effective SUV convergence, providing more accurate values²⁻⁴.

The behavior of Q.Clear it is controlled by a parameter β , included in the following penalty functions:

$$\Phi(x) = \sum_i y_i \log([Px]_i + r_i) - ([Px]_i + r_i) - \beta R(x) \quad (1)$$

$$R(x) = \sum_j \sum_{k \in N_j} w_{jk} \sqrt{\beta_j \beta_k} \frac{(x_j - x_k)^2}{x_j + x_k + \gamma |x_j - x_k|} \quad (2)$$

The parameter γ controls over the importance of the relative difference of pixels, to avoid an an oversmoothing, principally on the image edges⁵, although the unique possible user input parameter is the β .

- ¹ S. Ahn and J.A. Fessler, "Globally convergent image reconstruction for emission tomography using relaxed ordered subsets algorithms," *IEEE Trans. Med. Imaging* **22**(5), 613–626 (2003).
- ² S. Ahn *et al.*, "Quantitative comparison of OSEM and penalized likelihood image reconstruction using relative difference penalties for clinical PET," *Phys. Med. Biol.* **60**(15), 5733–5751 (2015).
- ³ J. Nuyts and J.A. Fessler, "A Penalized-Likelihood Image Reconstruction Method for Emission Tomography, Compared to Postsmoothed Maximum-Likelihood with Matched Spatial Resolution," *IEEE Trans. Med. Imaging* **22**(9), 1042–1052 (2003).
- ⁴ N. Parvizi, J.M. Franklin, D.R. McGowan, E.J. Teoh, K.M. Bradley, and F. V. Gleeson, "Does a novel penalized likelihood reconstruction of 18F-FDG PET-CT improve signal-to-background in colorectal liver metastases?," *Eur. J. Radiol.* **84**(10), 1873–1878 (2015).
- ⁵ J. Nuyts, D. Bequ??, P. Dupont, and L. Mortelmans, "A concave prior penalizing relative differences for maximum-a-posteriori reconstruction in emission tomography," *IEEE Trans. Nucl. Sci.* **49**(1 I), 56–60 (2002).

B. Jaszczak Phantom

In the context of this work, the Jaszczak phantom (Data Spectrum Corporation, Durham, NC, USA) was used in order to assess the image quality and resolution when different reconstructions are applied. This phantom is a cylinder fillable with water, with an internal diameter of 21.6 cm. The lower portion of the cylinder contains 6 sets of acrylic rods arranged in a pie-shaped pattern and with the following diameters: 4.8, 6.4, 7.9, 9.5, 11.1, and 12.7 mm. This allows the evaluation of spatial resolution in transaxial direction. The phantom was filled with a total activity of 25 MBq, providing a concentration of approximately 4.2 kBq/cm^3 , and acquired during 350 s. Then data was reconstructed using VHD, VPHD-S and Q.Clear algorithms, using a total of 70 cm FOV and the reconstruction parameters specified in the image quality section.

B. Supplemental results

Supplemental Table 1. Image quality comparison using NEMA NU2-2012 for different reconstruction algorithms (256x256 matrix) and a lesion-to-background of 2:1. Q.Clear with a β of 50, VPHD and VPHD-S using 12 subsets 8 iterations and a 2.0 mm gaussian filter.

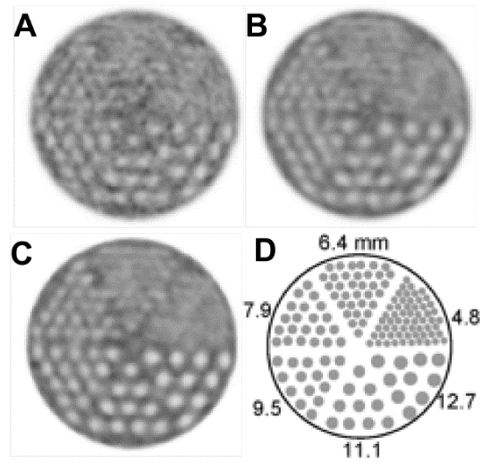
Sphere diameter (cm)	Contrast Recovery (%)			Background Variability (%)		
	VPHD	VPHDS	Q.Clear	VPHD	VPHDS	Q.Clear
10	27	27	34	9.8	9.0	5.8
13	53	55	65	7.9	7.7	4.6
17	75	76	86	6.0	6.0	3.6
22	83	84	90	4.8	4.7	2.9
28	70	74	82	4.3	4.4	2.7
37	75	79	85	3.9	3.2	2.9
Lung residual (%)	-	-	-	17.3	15.9	10.3

Supplemental Table 2. Image quality comparison using NEMA NU2-2012 for different reconstruction algorithms (256x256 matrix) and a lesion-to-background of 4:1. Q.Clear with a β of 50, VPHD and VPHD-S using 12 subsets 8 iterations and a 2.0 mm gaussian filter.

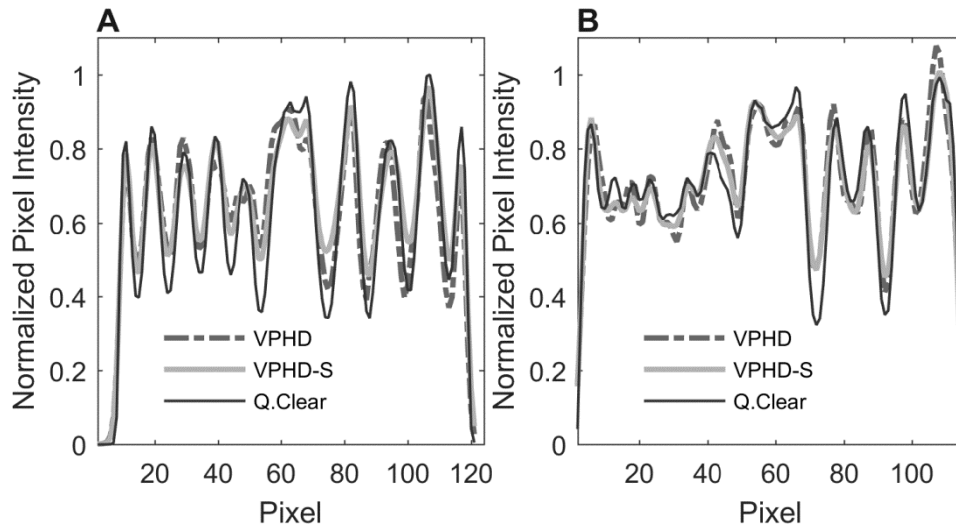
Sphere diameter (cm)	Contrast Recovery (%)			Background Variability (%)		
	VPHD	VPHDS	Q.Clear	VPHD	VPHDS	Q.Clear
10	53	56	62	9.3	8.9	8.0
13	53	63	68	7.8	7.5	6.7
17	65	76	75	6.1	6.0	5.3
22	75	79	83	4.6	4.5	4.1
28	69	70	80	3.5	3.4	3
37	74	74	84	3.1	3.1	2.9
Lung residual (%)	-	-	-	15.8	15.1	9.2

Supplemental Table 3. Image quality comparison using NEMA NU2-2012 for different reconstruction algorithms (256x256 matrix) and a lesion-to-background of 8:1. Q.Clear with a β of 50, VPHD and VPHD-S using 12 subsets 8 iterations and a 2.0 mm gaussian filter.

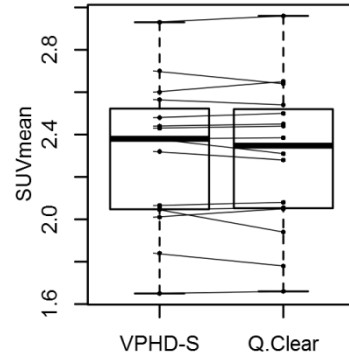
Sphere diameter (cm)	Contrast Recovery (%)			Background Variability (%)		
	VPHD	VPHDS	Q.Clear	VPHD	VPHDS	Q.Clear
10	44	45	60	8.3	7.8	5.8
13	53	55	65	6.6	6.5	4.6
17	66	67	86	5.5	4.7	3.6
22	73	79	90	4.4	4.1	2.9
28	67	69	82	3.4	3.3	2.7
37	74	80	85	3.4	3.3	2.9
Lung residual (%)	-	-	-	17.1	15.8	10.3



Supplemental Figure 1. Comparison of the Jaszczak phantom for the VPHD (A) ,VPHD-S (B) and Q.Clear (C) reconstructions, and (D) a cross-sectional schematic drawing of a Jaszczak phantom showing the position and diameter (in mm) of the 6 sectors of rods.



Supplemental Figure 2. Jaszczak phantom profiles, (A) horizontal, across 9.5 mm and 12.7 mm rods, and (B) vertical across, 6.4 mm and 11.1 mm rods, for VPHD, VPHD-S and Q.Clear reconstructions



Supplemental Figure 3. Quantitative analysis of the liver VOI for VPHD-S and Q.Clear reconstructions in terms of SUV_{mean} .